

REPORT DOCUMENTATION PAGE			Form Approved OMB NO. 0704-0188		
<p>The public reporting burden for this collection of information is estimated to average 1 hour per response, including the time for reviewing instructions, searching existing data sources, gathering and maintaining the data needed, and completing and reviewing the collection of information. Send comments regarding this burden estimate or any other aspect of this collection of information, including suggestions for reducing this burden, to Washington Headquarters Services, Directorate for Information Operations and Reports, 1215 Jefferson Davis Highway, Suite 1204, Arlington VA, 22202-4302. Respondents should be aware that notwithstanding any other provision of law, no person shall be subject to any penalty for failing to comply with a collection of information if it does not display a currently valid OMB control number. PLEASE DO NOT RETURN YOUR FORM TO THE ABOVE ADDRESS.</p>					
1. REPORT DATE (DD-MM-YYYY) 14-08-2017		2. REPORT TYPE Final Report		3. DATES COVERED (From - To) 1-Aug-2016 - 30-Apr-2017	
4. TITLE AND SUBTITLE Final Report: Droplet-Wall/Film Impact in IC Engine Applications (ARO Topic 1.4.1 under ARO's Dr. Ralph A. Anthenien)			5a. CONTRACT NUMBER W911NF-16-1-0449		
			5b. GRANT NUMBER		
			5c. PROGRAM ELEMENT NUMBER 611102		
6. AUTHORS			5d. PROJECT NUMBER		
			5e. TASK NUMBER		
			5f. WORK UNIT NUMBER		
7. PERFORMING ORGANIZATION NAMES AND ADDRESSES Princeton University PO Box 36 87 Prospect Avenue, Second Floor Princeton, NJ 08544 -2020			8. PERFORMING ORGANIZATION REPORT NUMBER		
9. SPONSORING/MONITORING AGENCY NAME(S) AND ADDRESS (ES) U.S. Army Research Office P.O. Box 12211 Research Triangle Park, NC 27709-2211			10. SPONSOR/MONITOR'S ACRONYM(S) ARO		
			11. SPONSOR/MONITOR'S REPORT NUMBER(S) 66511-EG-II.1		
12. DISTRIBUTION AVAILABILITY STATEMENT Approved for public release; distribution is unlimited.					
13. SUPPLEMENTARY NOTES The views, opinions and/or findings contained in this report are those of the author(s) and should not be construed as an official Department of the Army position, policy or decision, unless so designated by other documentation.					
14. ABSTRACT					
15. SUBJECT TERMS					
16. SECURITY CLASSIFICATION OF:			17. LIMITATION OF ABSTRACT UU	15. NUMBER OF PAGES	19a. NAME OF RESPONSIBLE PERSON Chung King Law
a. REPORT UU	b. ABSTRACT UU	c. THIS PAGE UU			19b. TELEPHONE NUMBER 609-258-5271

**RPPR Final Report**  
as of 12-Oct-2017

Agency Code:

Proposal Number: 66511EGII

**Agreement Number: W911NF-16-1-0449**

**INVESTIGATOR(S):**

**Name:** Chung King Law  
**Email:** cklaw@princeton.edu  
**Phone Number:** 6092585271  
**Principal:** Y

Organization: **Princeton University**

Address: PO Box 36, Princeton, NJ 085442020

Country: USA

DUNS Number: 002484665

EIN: 210634501

**Report Date:** 31-Jul-2017

Date Received: 14-Aug-2017

**Final Report** for Period Beginning 01-Aug-2016 and Ending 30-Apr-2017

**Title:** Droplet-Wall/Film Impact in IC Engine Applications (ARO Topic 1.4.1 under ARO's Dr. Ralph A. Anthenien)

**Begin Performance Period:** 01-Aug-2016

**End Performance Period:** 30-Apr-2017

**Report Term:** 0-Other

Submitted By: Chung King Law

Email: cklaw@princeton.edu

Phone: (609) 258-5271

**Distribution Statement:** 1-Approved for public release; distribution is unlimited.

**STEM Degrees:**

**STEM Participants:**

**Major Goals:** The objective of the proposed 9 month study is to determine the fate of droplets impacting a wet surface under various film thickness, which plays a critical role in controlling the efficiency of applications such as those associated with spraying in internal combustion engines (ICEs). Fuels sprayed inside engines can impact with the internal surfaces and thus not only obviates the purpose of atomization, but the subsequent film gasification also represents a completely different mode of fuel gasification that could fundamentally affect the fuel/air mixing and combustion processes including soot formation. The proposed program investigates the dynamics of droplet impaction on liquid film of various thicknesses simulating those within the ICEs. An existing apparatus will be upgraded to investigate the droplet-film impact event for various film thicknesses. Specifically, the droplets will be generated using a piezoelectric device or syringe-needle system. The dynamics will be studied for wide range of liquid alkanes and silicon oils to investigate the role of liquid properties on impact outcome. Moreover, the inter-facial gas-layer dynamics will be captured using high-speed interferometry.

**Accomplishments:** Uploaded as a separate file

**Training Opportunities:** The project involved experiments and simulation of drop impact on liquid film. The experiments and subsequent analysis were performed by a grad student and a research staff. All of them also participated in preparing the manuscripts with the PI.

The project not only enabled them to study the problem, they were also provided with opportunities to attend meetings and interact with colleagues and experts in the field, which are beneficial for their careers.

**Results Dissemination:** The outcomes of the project is presented in conferences. Two journal-quality papers are currently under review/preparation.

**Honors and Awards:** Nothing to Report

**Protocol Activity Status:**

**Technology Transfer:** Nothing to Report

**RPPR Final Report**  
as of 12-Oct-2017

**Report Type: Final Report**

Primary Contact E-mail: cklaw@princeton.edu

Primary Contact Phone Number: 609-258-5271

Organization /Institution name: Princeton University

**Award Information**

Grant/Contract Title: Droplet-Wall/Film Impact in IC Engine Applications

Grant/Contract Number: W911NF-16-1-0449

Principal Investigator Name: Prof. Chung K. Law

Program Manager: Dr. Ralph A. Anthenien

**Report Information: Final Report**

Reporting Period Start Date: August 1, 2016

Reporting Period End Date: March 30, 2017

## Report Abstract

Fuels sprayed inside IC-engines can impact the internal surfaces and thus obviates the purpose of atomization. Furthermore, the subsequent film gasification also constitutes a completely different mode of fuel gasification that could fundamentally affect the fuel/air mixing and combustion processes. The accumulation and growth of the film depends on the outcome of subsequent drop impact on the initially formed film, and as such controlling the outcome of the impact is critical for engine operation. In our recent study (Tang, et al., Soft Matter 2016), we presented a regime diagram based on the Weber number  $We$  (ratio of impact inertia and surface tension) and the film thickness, delineating the bouncing and merging operating conditions and providing scaling for the transition boundaries of a single liquid (C14 alkane). In this 9 month program, we have investigated the problem of drop impact on liquid film more closely and extracted fundamental understanding of the process which dictates the transition between merging and bouncing. Realizing that the liquid viscosity is a critical fluid property that fundamentally affects the impact outcome, through its influence on the fluid motion and viscous dissipation of the impact inertia, here we extend our previous study for liquids from C10 to C17 alkanes and additional silicon oils, covering a wide range of viscosity, to assess its effect on the regime diagram. We found that while the regime diagram maintains its general structure, the bouncing regime becomes smaller for less viscous liquids. Consequently viscous effects are modeled and a modified scaling is formulated.

Furthermore, we realized that the transition between merging and bouncing outcomes for drop impacting on a liquid film is critically controlled by the resistance from the microscopic interfacial gas layer trapped between the interacting and deformable drop and film surfaces. Using high-speed imaging and color interferometry, we have quantified and analyzed the gas layer dynamics during bouncing when the film thickness is comparable to the drop radius. Results show that the gas layer morphology changes dramatically and non-monotonically with the film thickness, and that in addition to the centrally located dimple previously observed for impact on thin films, a new, rim-dimple morphology is observed for larger film thicknesses. The effects of capillarity of the drop and film are also delineated by increasing the liquid viscosity and hence damping the respective surface waves. Two journal-quality papers are currently under review/preparation.

## Research Summary

### PART I: Bouncing to Merging Transition in Drop Impact on Liquid Film: Role of Viscosity

The efficiency of spraying in internal combustion engines (ICEs) is frequently complicated by droplet impaction on the cylinder walls in that the potential wall wetting not only obviates the purported advantage of atomization, but the subsequent film gasification also represents a completely different mode of fuel gasification that would fundamentally affect the fuel/air mixing and subsequent pollutant production [1]. Consequently, the fate the drops that subsequently impact the wetted surface is the key for growth or depletion of the deposited film. Specifically, bouncing of the impacted drops from the film would be beneficial in reducing localized fuel accumulation and soot formation. Thus, it is important to understand the mechanism that controls the transition between bouncing and merging outcomes upon a drop impact on a liquid film of various thicknesses. In our previous works [2, 3], we have explored the regime diagram of impacting outcomes, bouncing vs. merging, for nC14-alkane and have proposed scaling laws for transitional boundaries based on two non-dimensional parameters, the Weber number, defined as  $We = 2\rho V^2 R / \sigma$  and the nondimensional film thickness,  $H^* = H/R$ , where  $\rho$ ,  $\sigma$ ,  $V$ ,  $R$  and  $H$  are density, surface tension of liquid, impact velocity and radius of the drop, film thickness respectively. However, so far we have not considered the effect of viscosity which naturally plays a key role in the impact dynamics through dissipation. Previous studies on drop impact have shown that increase in viscosity would suppress splashing [4], levitate the spreading lamella [5], delay the merging time and increase the merging radius [6]. Recognizing the variation of viscosity of ICE fuels (gasoline or diesel) based on their sources, we herein explore the effect of viscosity on the transitional boundaries of the regime diagram and provide more comprehensive guidance in manipulating the impact outcomes.

In our experiment, the drop was generated by pushing liquid through a needle (using a syringe pump) and subsequently the drop first appeared and then detached from the tip of the needle when its weight overcame the capillary force. The falling drop landed on the liquid pool contained in a cubic glass-walled chamber with a 1.2mm thick microscope glass slide at the bottom. The drop generated was about 1.6mm in diameter. The impact velocity of the drop was controlled by changing the height of the needle from the impacted surface. Three liquids with varying viscosities were used. The full list of properties is given in Table 1. A monochromatic high-speed camera (Phantom V7.3) along with a 50mm lens (Nikon), a 2X tele-converter and an extension bellow were placed to capture the side-view shadowgraph of the falling drop using a high intensity halogen light for backlighting, operated at 15,037 frames per second (fps), with spatial resolutions of 17 $\mu$ m per pixel. The drop diameter, impact speed and liquid film thickness were measured by analyzing the side-view images from individual experiments.

Table 1: Properties for the liquids tested.

Liquid	Density ( $\text{kg/m}^3$ )	Surface tension (mN/m)	Kinematic viscosity (cSt)
Octane (C8)	708	21.1	0.69
Decane (C10)	730	23.8	2.37
Tetradecane (C14)	763	26.6	3.6
Heptadecane (C17)	777	27.5	4.76
Silicone Oil (S05)	913	20	5
Silicone Oil (S100)	966	20	100

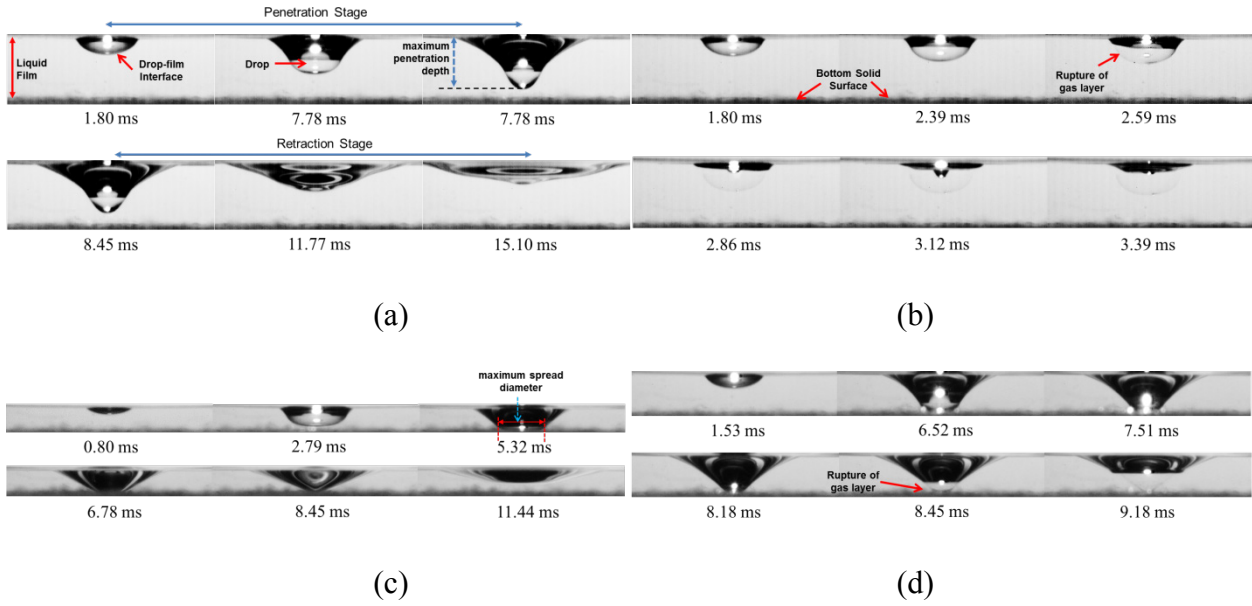


Figure 1: Typical impact events from the side-view. (a) Bouncing on a deep pool. (b) Early merging at similar film thickness but higher  $We$ . (c) Bouncing on a shallow pool. (d) Late merging at similar  $We$  but higher film thickness.

When a drop impacts a liquid film with comparable thickness, it can either bounce from or merge with the liquid surface. Typical time-resolved impact events for both merging and bouncing cases at a variety of film thicknesses are shown in Fig. 1. Fig. 1a shows bouncing at large film thickness, the drop does not reach the bottom solid wall where throughout the impact process. At similar film thicknesses, higher  $We$  (or impact inertia) leads to merging as the drop penetrates into the liquid film (Fig. 1b). For smaller film thicknesses, although the drop still

bounces, it actually reaches the solid wall and spreads over it before leaving the surface (Fig. 1c). For similar  $We$ , but at intermediate film thickness, when the drop retracts after spreading on the solid wall, it merges with the liquid surface, leading to “late” merging (Fig. 1d). The regime diagram for C14 of the aforementioned impact outcomes in the  $We-H^*$  space is shown in Fig. 2a, where early merging (black solid circle) occurs at high  $We$  ( $>15$ ) across all film thicknesses and late merging (black open circle) occurs at intermediate  $We$  for intermediate film thicknesses, and the rest is bouncing (grey square). In [3] we have identified the controlling physics of the transition boundaries for these impact outcomes, namely *Inertial Limit* which separates the early merging from bouncing, *Deep Pool Limit* and *Deformation Transition* which define the upper and lower boundaries of the late merging respectively, and *Thin Film Limit* which defines the thin film merging zone. Previously, viscosity effect was neglected in the scaling of these boundaries, but would affect the scaling through dissipation loss, which is the focus of this study.

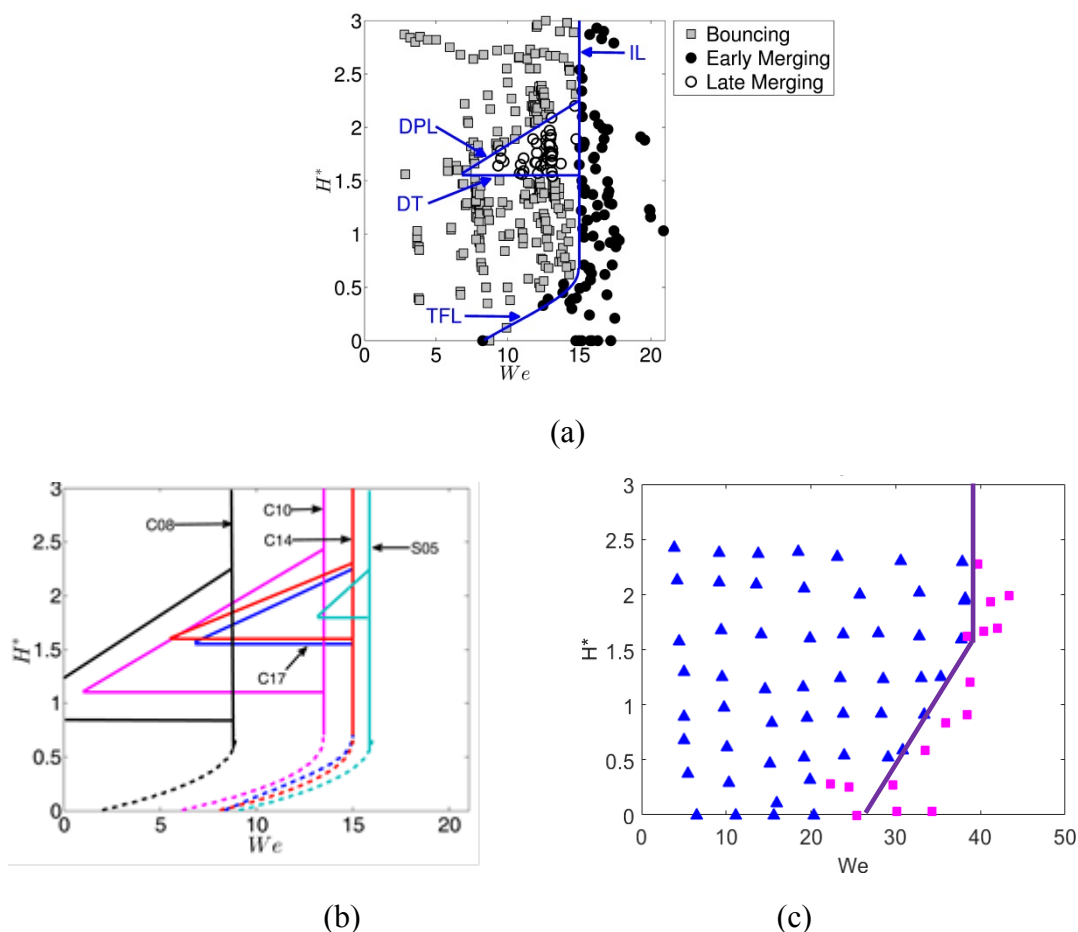


Figure 2: Regime diagrams of bouncing-merging impact outcomes for liquids with varying viscosity. (a) C14 alkane. The data points are the impact outcomes. The lines are transition boundaries: IL: Inertial Limit, DPL: Deep Pool Limit, DT: Deformation Transition. TFL: Thin Film Limit. (b) Regime diagram all liquids tested except S100. (c) Regime diagram for S100.

We have tested liquids with a large range of kinematic viscosity ranging from 0.69 to 100 cSt. Figure 2 shows the response of the regime diagram to the changing viscosities. Globally, the merging zone shrinks with increasing viscosity: the critical  $We$  for the *Inertial Limit* increases and the *Thin Film Limit* moves to the right, reducing the area of early merging; while the *Deep Pool Limit* shifts downward and the *Deformation Transition* moves upward, diminishing the late merging zone. Phenomenologically, this is expected since the major role of viscosity is dissipating energy which reduces the effective kinetic energy that brings the drop and impacted liquid film surface close enough to induce merging. Thus, with increasing viscosity, the effective kinetic energy becomes weaker rendering merging to be difficult. The detailed mechanisms are discussed in the following sections.

### *Inertial Limit*

The *Inertial Limit* constitutes the transition between bouncing and “early” merging, which occurs when the impact inertia during the penetration process breaks the interfacial gas layer to induce merging. Mechanistically, when the drop impacts the liquid film with enough inertia, it can overcome the resistance due to the pressure build-up in the interfacial gas layer, and locally succeeds in bringing the interfaces close enough for the van der Waals force to effect merging. The critical gas layer thickness  $d_{cr}$  for merging to occur is around 200nm [7-10]. Bouwhuis *et al.* [11] proposed a scaling analysis predicting the dependence of the maximum dimple height, a characteristic thickness of the gas layer, on the impact velocity for drop impact on dry surfaces, which was later adopted successfully for drop impacting liquid pool by Tran *et al.* [6]. According to this scaling, the maximum dimple height of the air layer depends on the Stokes number, which corresponds to the relation,  $d \sim U_p^{-2/3} R^{1/3} \rho^{-2/3} / \mu_g^{-2/3}$ , where  $d$  is the dimple height,  $U_p$  the penetration velocity which is the speed at which the drop moves into the liquid film, and  $\mu_g$  the dynamic viscosity of the surrounding gas. The critical penetration velocity that reduces the gas layer thickness to the critical value  $d_{cr}$  is thus:

$$U_{p,cr} \sim \frac{\mu_g R^{1/2}}{\rho} d_{cr}^{-3/2} \quad (1)$$

It is noted that the process of merging through the collapsing gas layer is restricted to a localized zone around the interface and thus does not depend on the global parameters such as the liquid film thickness. However, the film thickness can alter  $U_p$ , which is significantly different from  $U$ . As the drop impacts the liquid film, it simultaneously deforms and pushes the liquid inside the film, converting part of its kinetic energy to the surface and kinetic energies of the deformed film. The merging in this regime generally occurs very early in the penetration process, inhibiting significant deformation of the drop and the liquid film. Thus for simplicity we can ignore the changes in the drop and liquid film surface energy. Moreover, Tran *et al.* [6] showed that the penetration processes for liquids with various viscosities indeed are very similar, demonstrating the weak role of viscous dissipation in these processes. To analyze the energy

conversion, for impact on liquid film with large thickness ( $H^* > 1$ ), one can assume the movement of the drop into the film generates a radial potential flow around the drop, as illustrated in Fig. 3a where the flow velocity  $V$  in the film scales as  $V \approx U_p R^3 / r^3$ , at distance  $r$  radially from the drop center. To evaluate the induced kinetic energy in the film,  $(K_E)_F$ , we integrate the kinetic energy of the infinitely small shell with thickness  $dr$  at radius  $r$ , within the liquid film,

$$(K_E)_F = \int_R^\infty 2\pi\rho r^2 V^2 dr \approx \int_R^\infty 2\pi\rho r^2 \left( U_p R^3 / r^3 \right)^2 dr \approx 2\pi\rho U_p^2 R^3 \quad (2)$$

Balancing the drop kinetic energy before the impact,  $(K_E)_{D,0} = 2\pi\rho R^3 U^2 / 3$ , with the total kinetic energy of the drop,  $(K_E)_D = 2\pi\rho R^3 U_p^2 / 3$ , and the film,  $(K_E)_F = 2\pi\rho R^3 U_p^2$ , during the penetration process yields

$$U_p / U \approx 1/2 \quad (3)$$

Both in our experiment and literature [Tran *et al.*, 2013],  $U_p$  is found to be about half of  $U$ . It is important to note that this relationship does not depend on  $H^*$ . Combining equations (1) and (3), we arrive at a critical impact velocity and the corresponding critical  $We$  which is the measure of minimum impact inertia required for merging, defining the *inertial limit* as,

$$U_{cr} \approx \frac{2\mu_g R^{1/2}}{\rho} d^{-3/2} \quad (4a)$$

$$We_{cr} \approx \frac{4\mu_g^2 R^2}{\rho^2 \sigma} d^{-3} \quad (4b)$$

It is seen that  $We_{cr}$  does not depend on the liquid film thickness and thus appears as a vertical line in the regime diagram (shown in Fig 1a). The transition from bouncing to merging across this limit is solely controlled by the impact inertia.

Now, if we consider the liquids with various viscosities, we find that the measured  $We_{cr}$  depends on kinematic viscosity with a power law of 0.3 (Fig 3b). To theoretically model the viscous loss, we consider the viscous loss in the Boundary layer around the droplet surface. The boundary layer thickness can be approximated as  $\delta \approx \sqrt{1 / Re_L}$ , where  $Re_L = \sqrt{\nu / (U_p R)}$  using analogy to flat plate. Further analysis shows the energy loss through drag friction drag in the boundary layer is force is  $E_\phi \approx (\rho U_p^2 R^3) \sqrt{1 / Re_L}$ . So rewriting the energy balance with viscous

dissipation,  $KE_{D,0} = KE_F + KE_D + E_\phi$  which translates to  $\frac{We}{We_p} \approx 4 + C \frac{1}{\sqrt{Re_L}} \approx \nu^{1/2}$ , where C is a

dimensionless factor. The scaling captured the qualitative dependence on viscosity reasonably well, albeit with stronger dependence (theory,  $\nu^{0.5}$  vs experiments,  $\nu^{0.3}$ ). We attribute the deviation on the curvature of the drop surface, while we assume flat geometry.

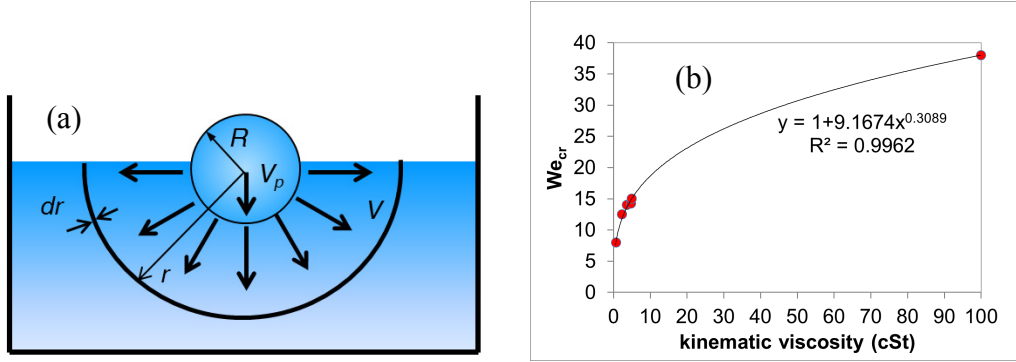


Figure 3: Inertial Limit: (a) schematic of the flow field induced by the drop inside the liquid film. (b)  $We_{cr}$  of Inertial Limit as a function of  $\nu$ .

### Deformation Transition Limit

As identified in [3], *Deformation Transition* occurs at the intermediate film thickness where increase in film thickness causes a “delayed” merging. Mechanistically, in this regime the drop deforms the film and itself as it reaches the full depth of the film and spreads against the solid surface. On the rebound process, this “late” merging can occur if the liquid surface moves faster than the drop as they both retracts. It is inherently controlled by the ratio of the available surface energy (or surface area) of the liquid film and the drop at the end of the penetration process. When the ratio exceeds a critical value, the liquid surface attains a retraction speed large enough to merge with the drop. The ratio is measured in terms of the surface area from the side-view images and for C14 shown in Fig. 4a as a function of  $We$ , which shows no obvious dependence, indicating that the *Deformation Transition* is a constant  $H^*$  line. To estimate this energy budget, the deformed liquid film is modeled as a cylinder with radius  $w$  and height  $H$  and the deformed drop as a cylinder with radius  $w$  and height  $H_d$ , as shown in the schematic in Fig. 4b.

Comparing the surface energy between the drop and the liquid film shows that the critical film thickness for the bouncing-merging transition depends only on the spread width  $w$ . If  $w < w_{cr}$ , late merging happens. If we plot  $w^*$  ( $=w/R$ ) vs  $H^*$  (Fig 4c) we see a linearly decreasing trend, since with increase in the film thickness the resistive influence from the bottom solid surface decreases and thus the drop does not spread as much. Interestingly, if we plot  $w^*$  vs  $H^*$  for different viscosities, they follow the same linear relationship, signifying weak viscous effect on the spreading process (at least around this film thickness range). However, after spreading when the film retracts, the upward momentum gained will be reduced by viscous loss, and as such for higher viscosity it would require higher momentum and thus higher deformed surface energy for merging. Recognizing that higher deformed film surface is marked by weaker drop deformation or lower  $w^*$ , we expect the merging transition to occur at higher  $H^*$ , which we also find experimentally (Fig. 4d).

Now to model the viscous dissipation that affects this transition, we only consider the dissipation in the film associated with the rebounding stage. Since both the liquid film and drop retracts from the maximum spreading diameter, the kinetic energy comes from the surface energy minus the dissipation. The energy balance thus suggests that the ratio between  $\Delta SE_f - E_\Phi$  and  $\Delta SE_d$  is larger than a critical value, late merging happens. Based on the schematic of the shapes at maximum deformation as shown in Fig. 4b,  $\Delta SE_f \approx \sigma(2\pi wH)$  and  $\Delta SE_d \approx \sigma(2\pi w^2 + 2\pi wH_d) - \sigma(4\pi R^2)$ . Since the rebounding process of the deformed resembles capillary wave, we evaluate the viscous loss in capillary processes to estimate the dissipation. Following in classical text books [12], we arrive at  $E_\Phi = E_0(1 - e^{-2\eta\Delta t})$ , where  $E_0$  is initial energy,  $\Delta t$  is elapsed time and  $\eta = 2\nu / R^2$ . For the rebounding process using  $E_0 = \Delta SE_f$  and  $\Delta t \sim (\rho R^3 / \sigma)^{1/2}$  one can show that  $H_{cr} \approx (w^*)e^{2\nu\rho R/\sigma}$ , which suggests an exponential dependence of  $H_{cr}^*$  with  $\nu$  as seen in the experiments (Fig. 4d).

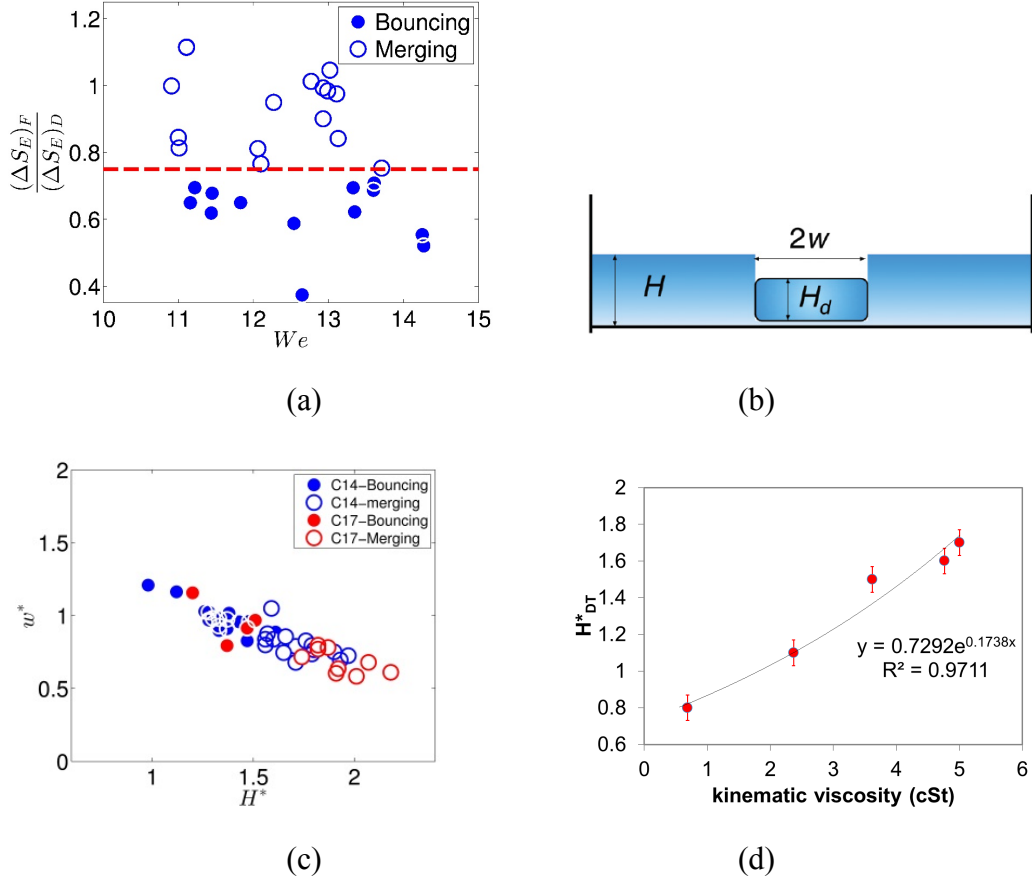


Figure 4: Viscosity effect on the Deformation Transition. (a) Ratio of the available surface energy of the liquid film and the drop as a function of  $We$ . (b) Schematic of the model for the drop and liquid film deformation at maximum spread diameter. (c) Plot of  $w^*$  as a function of  $H^*$  for all liquids tested. (d) Deformation Transition  $H_{cr}^*$  for different viscosities.

## Deep Pool Limit

The *Deep Pool Limit* is defined as  $H^* = h_{p \max}^*$ , where  $h_{p \max}^*$  is the maximum penetration depth of the drop into the liquid pool (Fig 1a). Physically, if the drop cannot reach the bottom solid surface during penetration, the late merging mechanism is not realizable and the drop will bounce. Theoretically,  $h_{p \max}^*$  is determined by assuming the drop does not change shape when it reaches the maximum penetration and the initial kinetic energy is converted to the increase of the liquid pool surface energy as well as dissipated. By carrying out the energy balance, the  $h_{p \max}^*$  is found to be linearly dependent on  $We$ , which is proven by the experimental results (Fig. 5a) for all liquids used. The slope ( $m$ ) of the linear dependence is extracted and plotted as a function of  $\nu$  in Fig. 5b, which shows a decreasing trend with increasing viscosity. Phenomenologically, larger viscosity results in larger viscous dissipation and thus the effective kinetic energy to penetrate downward becomes less, reducing the penetration depth.

To model the problem, we consider the energy balance from the instant of the drop impact till it reaches the maximum penetration  $KE_{D,0} = KE_F + \Delta SE_F + E_\phi$ , where  $KE_{D,0} = 2\pi\rho R^3 U^2/3$  is the initial drop kinetic energy,  $KE_F = 2\pi\rho R^3 U_p^2 = \pi\rho R^3 U^2/2$ ,  $\Delta SE_F \approx \sigma[2\pi R\{(h_p)_{\max} - R\} + 2\pi R^2]$  is the increase in the liquid film surface energy, and  $E_\phi$  is the energy loss in viscosity. If we follow the boundary layer assumption used for inertial limits, we arrive at  $E_\phi \approx (\rho U^2 R^3) \sqrt{1/\text{Re}_L}$ . By balancing the terms in energy equation we get  $H^* \approx (C_1 - \frac{C_2}{\sqrt{\text{Re}_L}})We$ . So we obtain a linear dependence of the penetration depth with  $We$  and we also see that the slope changes with viscosity as  $m \approx C_1 - C_2\sqrt{\nu}$ , which fits the experimentally obtained data well.

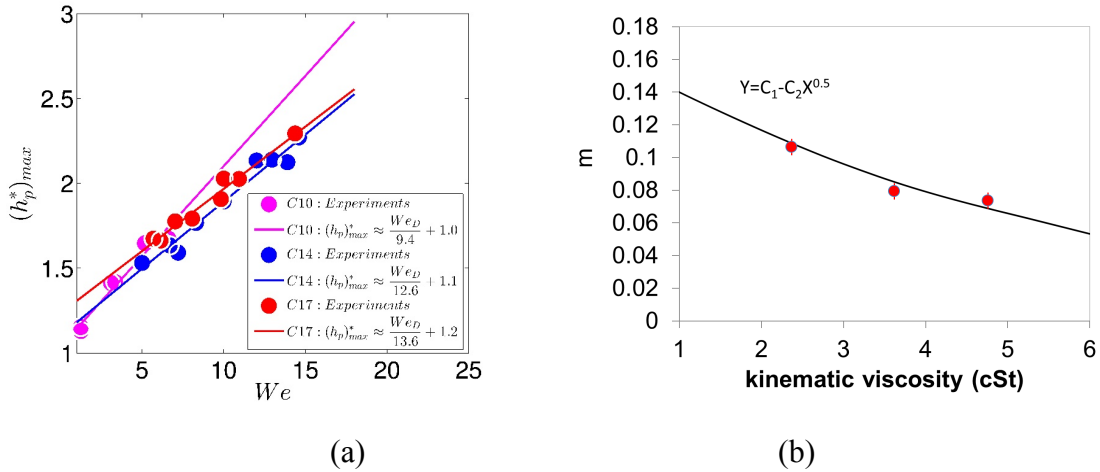


Figure 5: Viscosity effect on the Deep Pool Limit. (a)  $h_{p \max}^*$  as a function of  $We$  for all liquids tested. (b)  $dh_{p \max}^*/dWe$  as a function of  $\nu$  for all liquids tested.

Through the influences on the *Deep Pool Limit* and the *Deformation Transition*, it is clear that viscosity has a diminishing effect on the “late” merging zone, and as such at a certain viscosity the two limits will merge to *engulf* the “late” merging zone, as is shown in Fig. 2c for liquid of 100 cSt.

In summary, we have investigated the bouncing to merging transition for drop impact on liquid film at various viscosities, and found that through dissipation, higher viscosity renders merging more difficult and as such shrinks the merging regime. The detailed viscous effect on each transition boundary is analyzed and explained. This provides a more comprehensive guidance for predicting the bouncing-merging transition when a drop impact on a liquid film.

## References

- [1] R. D. Reitz, Directions in internal combustion engine research, *Combust. Flame* 160 (2013) 1-8.
- [2] K. L. Pan, C. K. Law, Dynamics of droplet-film collision, *J. Fluids Mech.* 587 (2007) 1-22.
- [3] X. Tang, A. Saha, C. K. Law, & C. Sun, Nonmonotonic response of drop impacting on liquid film: mechanism and scaling. *Soft matter* 12 (2016) 4521-4529.
- [4] A. L. Yarin, Drop impact dynamics: splashing, spreading, receding, bouncing...., *Annu. Rev. Fluid Mech.* 38 (2006) 159-192.
- [5] C. Josserand, & S. T. Thoroddsen, Drop impact on a solid surface, *Annu. Rev. Fluid Mech.* 48 (2016) 365-391.
- [6] T. Tran, H. de Maleprade, C. Sun, & D. Lohse, Air entrainment during impact of droplets on liquid surfaces. *J. Fluids Mech.* 726 (2013) R3.
- Couder *et al.* (2005), Thoroddsen *et al.* (2012), Hicks & Purvis (2011), Li *et al.* (2015)
- [7] Y. Couder, E. Fort, C.H. Gautier & A. Boudaoud, From bouncing to floating: Noncoalescence of drops on a fluid bath. *Phys. Rev. Lett.* 94, 177801 (2005).
- [8] P.D. Hicks & R. Purvis, Air cushioning in droplet impacts with liquid layers and other droplets. *Phys. Fluids.* 23, 062104 (2011).
- [9] M. Li, A. Saha, D.L. Zhu, C. Sun & C.K. Law, Dynamics of bouncing-versus-merging response in jet collision. *Phys. Rev. E* 92, 023024 (2015).
- [10] S.T. Thoroddsen, M.J. Thoraval, K. Takehara, & T.G. Etoh, Micro-bubble morphologies following drop impacts onto a pool surface. *J. Fluid Mech.* 708, 469-479 (2012).
- [11] W. Bouwhuis, R.C. van der Veen, T. Tran, D.L. Keij, K.G. Winkels, I.R. Peters, & D. Lohse, Maximal Air Bubble Entrainment at Liquid-Drop Impact. *Phys. Rev. Lett.* 109, 264501 (2012).
- [12] E. Lifshitz and L. Landau, *Course of Theoretical Physics, Fluid Mechanics*, 1959, vol. 6.

## PART II: Bouncing Drop on Liquid Film: Dynamics of Interfacial Gas Layer

Drop impact on wet or dry surfaces may result in either merging [1–6] or bouncing [7–11] of the impacting interfaces. The controlling factor is whether the thin gas layer trapped between the impacting surfaces can resist the impact inertia to bring them to close proximity for the van der Waals force to effect merging. However, due to the microscopic nature of this gas layer, it is difficult to experimentally observe the morphology and dynamics of the interfaces. Recently optical techniques such as interferometry [4, 10–16] and internal reflection microscopy [3, 9] have been developed to indirectly interpret the gas layer thickness for drop impact on solid surfaces. Such studies have mostly been concerned with the merging outcomes [3, 4, 12, 15, 17], while corresponding studies on the morphology of the gas layer for the bouncing outcomes have been few. Only recently, de Ruiter *et. al.* [11] showed that, for a bouncing drop on a solid surface, a bell-shaped dimple develops at the center and maintains its shape throughout the impact until the drop departs from the solid surface. However, the superficially analogous problem of drop bouncing from a liquid film and the associated interfacial gas layer dynamics has not been investigated. Phenomenologically, while drop impact on a solid surface involves only one deformable surface and the internal dynamics of the drop, two deformable surfaces are involved for impact on a liquid film, with the additional film surface participating not only in the much richer dynamics of the gas layer, but also through the internal dynamics of the film itself.

A critical system parameter controlling the impact response is the film thickness which offers the resistance from the submerged solid surface. Previous studies have been mostly concerned in the limiting situations of either a solid surface [1–4, 7–16, 18], hence vanishing film thickness such that the drop motion is totally restricted by the rigid surface, or a deep liquid pool [5, 19–24] representing infinite film thickness such that the drop motion is controlled by the deformable pool surface. Less study, however, has been directed to the intermediate situation [25, 26] for which the film thickness is comparable to the drop radius, such that the resistance of the solid wall is closely felt, while the morphologies of the drop and film are also strongly coupled through the interfacial gas layer. Such situations are of particular technological relevance, including spray coating and 3D printing, in which drops impact on a liquid layer generated by previously deposited drops.

In this project, we have studied, for the first time, a complete temporal characterization of the gas layer dynamics for drop bouncing on liquid surface with thickness comparable to the drop radius, using high-speed imaging and color interferometry. We have succeeded in identifying the role of the nondimensional film thickness ( $H^* = H/R$ ) and Weber number ( $We$ ) in controlling the gas layer morphology, where  $We = 2\rho RU^2/\sigma$ ,  $\rho$ ,  $R$ ,  $U$ ,  $\sigma$  are the density, radius, velocity, and surface tension of the drop, and  $H$  is the film thickness. In particular, we shall show that the presence of the deformable impacted surface drastically modifies the shape

and evolution of the thin gas layer, as observed previously for the impact on solid surfaces.

Experimentally, a drop of about 1.6 mm diameter was generated by pushing the test liquid through a vertically-oriented stainless-steel needle using a syringe pump, with the drop separating from the needle tip when its weight overcame the capillary force. The drop landed on a liquid film contained in a  $25 \times 25 \times 10 \text{ mm}^3$  chamber with a 1.2 mm thick microscope glass slide at the bottom. The impact speed was changed by manipulating the distance between the needle and the impacted surface. Tetradecane ( $\rho$ :  $760 \text{ kg}\cdot\text{m}^{-3}$ ,  $\sigma$ :  $27 \text{ mN}\cdot\text{m}^{-1}$ , kinematic viscosity,  $\nu$ :  $3.6 \text{ cSt}$ ) was used as the working fluid for both the drop and liquid film.

A high-speed camera (Phantom V7.3) along with a 50 mm lens (Nikon) and a 2X tele-converter was used to capture the side-view shadowgraph images of the impact, with the aid of a halogen light. In addition, a high-speed color camera (Phantom V710) with a microscope system (Navitar 6000) connected to a 5X objective (Mitutoyo) and a coaxially ported broadband white light (Olympus ILP2) was used to capture the bottom-view interference pattern created by the gas layer between the drop and film surfaces. The gas layer thicknesses were extracted by comparing it with a known reference profile of a lens. Details of this high-speed color interferometry are given in Reference [12]. All the images were recorded at 15,037 fps, with spatial resolutions of  $17 \text{ }\mu\text{m}/\text{pixel}$  for the side-view images and  $0.75 \text{ }\mu\text{m}/\text{pixel}$  the bottom-view images. The instantaneous drop diameter, impact speed, and liquid film thickness were measured from the side-view images.

Based on the film thickness, the bouncing response can be divided into three regimes: namely thin film ( $H^* < 1$ ), thick film ( $1 < H^* < 1.5$ ) and deep pool ( $H^* > h_{\text{max}}^*$ ). [26] The thin film regime bears close resemblance to impact on solid surface since the effect of the rigid surface is prominent despite the presence of a thin layer of liquid.  $H^* = h_{\text{max}}^*$  [26] constitutes the deep pool limit, where  $h_{\text{max}}^* = 1 + We/12$  is the normalized maximum penetration of the drop into the liquid pool. Thus for the deep pool, the drop is far from the bottom surface during impact, and as such the gas layer dynamics is only affected by the drop and the liquid surface. In between these two extremes in the thick film regime, the process is influenced by both the resistive solid surface and the adaptive liquid film. While there is no clear discernable boundary between the thin and thick film regimes, it is reasonable to identify that the transition occurs when the film thickness is close to the drop radius, *i.e.*  $H^* \approx 1$ .

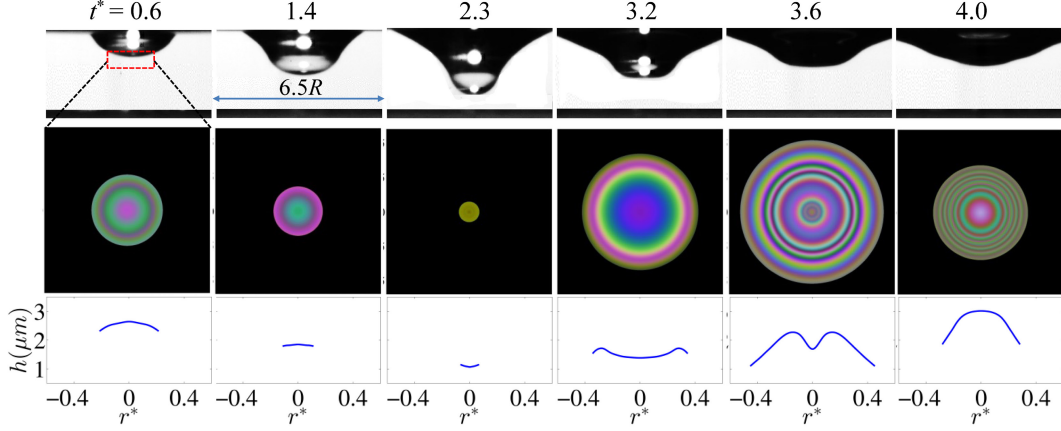


**FIG. 1:** Global impact dynamics from side-view (top row), local dynamics of interfacial gas layer from bottom-view interference fringes (middle row) and corresponding thickness profiles (bottom row).  $R =$  drop radius.  $r^* = r/R$ . Time is normalized by the inertial time scale  $t^* = t/(2R/U)$ .  $We=12.96$ ,  $H^*=2.67$ .

A typical bouncing event is shown in Fig. 1, where the top row consists of the side-view images (global behavior), while the middle and bottom rows show the interference patterns and the corresponding gas layer thickness profiles. Figure 2a shows the schematic of the gas layer globally and locally, with  $h_c$  being the center thickness of the axisymmetric gas layer, and  $h(r)$  the radial variation. The gas layer dynamics will now be discussed in terms of the evolution of  $h_c$  and  $h(r)$ .

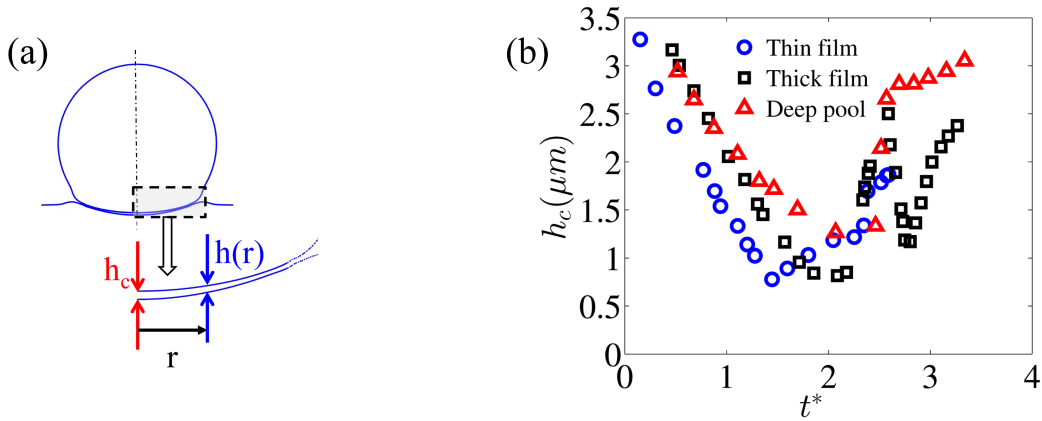


**FIG. 2:** (a) Schematic of the gas layer and definitions of center thickness  $h_c$  and radial variation  $h(r)$ . (b) Gas layer center thickness evolution for three different film thicknesses with similar  $We$  numbers. Blue circle:  $We=9.91$ ,  $H^*=0.12$ . Black square:  $We=8.04$ ,  $H^*=1.19$ . Red triangle:  $We=9.26$ ,  $H^*=2.72$ .

We first consider the evolution of  $h_c$ , with time normalized by the inertial timescale,  $2R/U$ , in Fig. 2b. Here  $t^* = 0$  represents the instant when the bottom of the drop reaches the location of the unperturbed liquid surface. There are two distinct stages: the approaching stage, when the gap at the center continuously diminishes to reach a minimum point; and the rebounding stage,

when the gap increases. During the approaching stage, for all  $H^*$ ,  $h_c$  decreases linearly with time with almost the same slope and a slightly smaller slope for the deep pool. During the rebounding stage, however, the response is dramatically different in that while the rate of increase of  $h_c$  is rather steady for the thin film, for the deep pool it first increases rapidly and then slows down substantially. For the intermediate case of the thick film,  $h_c$  responds non-monotonically by first sharply jumps to a value of  $2.5 \mu\text{m}$ , then immediately drops to  $1 \mu\text{m}$ , and then increases again within a very short  $t^*$  (increment of about 0.5).

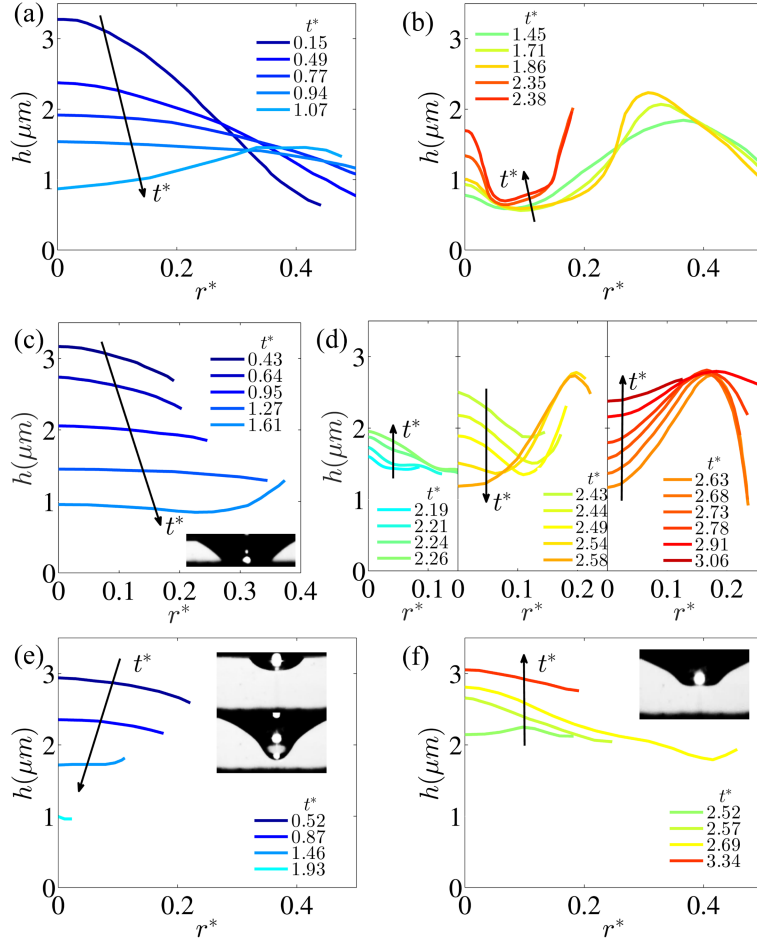


**FIG. 3:** Gas layer thickness profiles at approaching (a, c, e) and rebounding (b, d, f) stages. (a) (b) Thin film,  $We=9.91, H^*=0.12$ . (c) (d) Thick film,  $We=8.04, H^*=1.19$ . (e) (f) Deep pool,  $We=9.26, H^*=2.72$ .

Next we discuss the instantaneous radial variation of the gas layer thickness and its evolution for all the three conditions (Fig. 3); the left and right columns respectively indicate the approaching and rebounding stages. For the thin film, as the drop approaches the liquid surface, it squeezes the interfacial gas layer and hence creates a high-pressure zone, which in turn deforms both the drop and film surfaces and forms a bell-shaped gap with the center elevated relative to the rim (Fig. 3a). This is analogous to the well-known dimple formed at the center when a drop impacts a solid surface, except now the interfacial gap for the thin film is

formed from the deformation of both the drop and film surfaces. The trapped gas layer is subsequently squeezed out as the drop moves down further. This is evident from the flattened and even reversed profile with elevated rim relative to the center and a minimum thickness reaching below  $1 \mu m$  before the rebounding stage begins; recognizing that a typical gas layer thickness just before merging is about  $200 \text{ nm}$  [19, 20, 27]. For the deep pool (Fig. 3e), although the shape of the center dimple is maintained, the gas layer thickness profiles are flatter and shorter. Due to the large pool thickness and the diminished constraint from the solid surface, the deformable liquid surface is more adaptive to the drop impact, thereby reduces the radial variation in the gas layer thickness and hence the pressure gradient. The unrestrained deformation in the liquid surface also results in a steeper interface (side-view image in inset of Fig. 3e), deflecting the incident light from the bottom away from the camera, which progressively reduces the extent of the measured profile as the drop penetrates the liquid pool. For the thick film, the gas layer thickness profiles (Fig. 3c) show a mixed influence of the deep pool and thin film regimes, in that the profile is flatter due to the adaptive liquid surface and its radial extent increases with time due to spreading against the bottom surface.

During the rebounding stage for the thin film, when the drop as a whole rises upward (Fig. 3b), the center of the gas layer gradually thickens, forming another, albeit much narrower, bell-shaped profile. At the same time, the rim also thickens forming an annular dimple, and is connected to the center dimple with a thin neck ( $0.5 \mu m$ ). Both dimples become thicker as the drop moves upward during the rest of the rebounding stage, with the neck moving inward and becoming thicker. Note that the radial extent of the visible interference pattern and thus, measured gas layer thickness, reaches beyond  $r^* = 0.5$ . Mechanistically, deformation of the liquid surface is now largely constrained by the solid surface such that spreading of the drop over the surface closely resembles drop impact on the dry surface. For the deep pool (Fig. 3f), the center thickens first but with a flatter profile. The gas layer becomes thicker as the drop leaves the liquid surface without changing its shape. The observable extension is now larger, up to  $r^* = 0.5$ , as compared to the approaching stage.

For the thick film, however, evolution of the profiles is markedly different (Fig. 3d). At the beginning of the rebounding stage, the center of the gas layer thickens, with the familiar bell-shape dimple. It then changes immediately within  $0.28 \text{ ms}$  ( $\Delta t^* = 0.7$ ), as the profile becomes flatter and thinner at the center with a thicker rim forming a *reverse bell-shape*, with the rim being thicker than the center. Finally, with the rim remaining the same, the center starts to become thicker and approaches the thickness of the rim until the drop leaves the liquid surface. The unaltered rim thickness during the latter part of the rebounding stage indicates that shape oscillation of the drop and relaxation of the stretched/deformed film surface are phase matched, and as such they move together near the rim. Such complex behavior of the gas layer dynamics arises from the interplay of the deformation and relaxation of the drop and film surfaces along with the resistance from the solid wall, which is specific for the thick film.

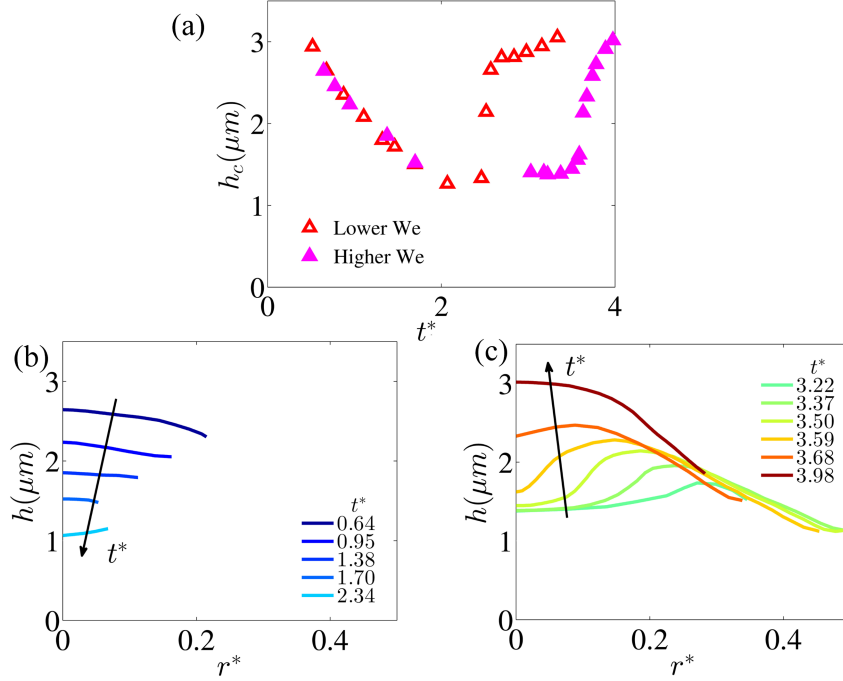


**FIG. 4:** Gas layer dynamics for deep pool with higher  $We$ .  $We=12.96$ ,  $H^*=2.67$ . (a) Comparison of center thickness evolution for lower (9.26) and higher (12.96)  $We$ . Gas layer thickness profiles at (b) approaching and (c) rebounding stages.

To evaluate the effect of  $We$ , evolution of the center thickness,  $h_c$ , (Fig. 4a) and the radial variation,  $h(r)$ , (Figs. 3e-f vs 4b-c) of the gas layer for the deep pool are compared for two different values of  $We$ . For the evolution of  $h_c$ , the slope of the linear approaching stage and the general behavior of the monotonic rebounding stages are the same for both  $We$ . However, for higher  $We$ , there is a delay between the end of the approaching stage and increase of the center thickness. The gas layer thickness profiles during the approaching stage are also similar with the predominant flat profile and reduced radial extension. During the rebounding stage at higher  $We$  (Fig. 4c), unlike previous conditions, the rim becomes thicker first and develops an “annular dimple”, which grows and starts propagating towards the center because of the radially inward entrainment of gas from outside. Finally, the dimple arrives at the center as the profile takes a bell-shape and is maintained until the drop leaves the liquid surface. This specific characteristic, which appears only at higher  $We$ , likely arises from a phase mismatch between relaxation of the deformed film and the oscillating drop. Although the drop relaxation is solely controlled by its own capillarity, inception of the relaxation process for the liquid surface can only occur after it reaches maximum deformation. Both the duration and degree of the deformation depend on  $We$ , affecting the phase delay between the drop and the liquid surface.

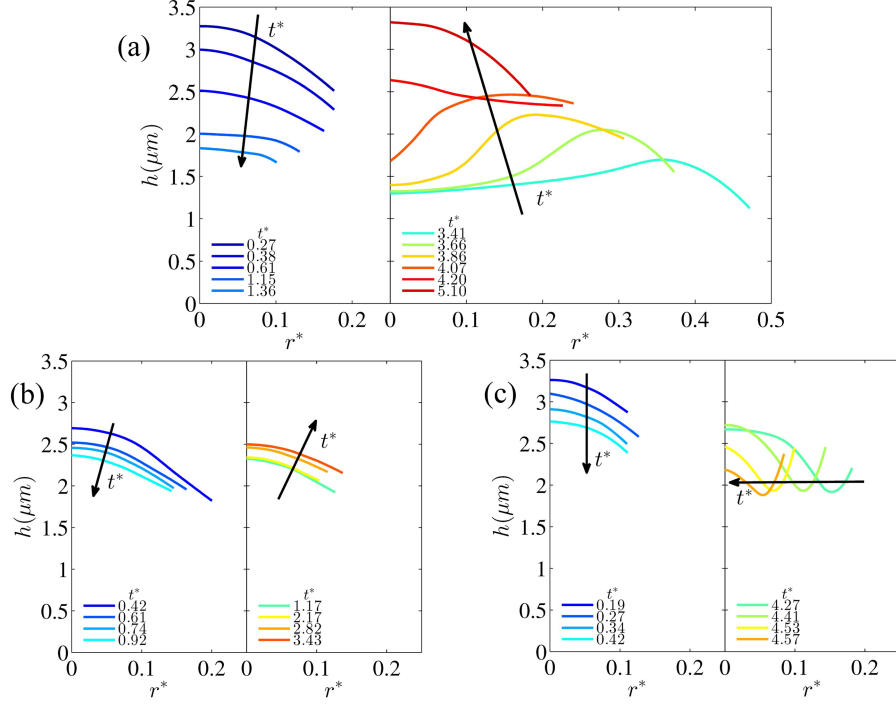


**FIG. 5:** Gas layer thickness profiles at approaching (left panels) and rebounding (right panels) stages for higher viscosity liquids. (a) Drop (C17)/Film (C17),  $We=13.31$ ,  $H^*=2.2$ . (b) Drop (S100)/Film (S100),  $We=13.73$ ,  $H^*=2.37$ . (c) Drop (S100)/Film (S5),  $We=12.77$ ,  $H^*=2.81$ .

Unlike impact on flat solid surface where the gas layer thickness profile directly depicts the local shape of the drop, for drop impact on liquid film, it is the relative distance between the deformed surfaces of the drop and the film. To understand which contributes more towards the observed gas layer dynamics: the drop or the film surface, we performed additional experiments with liquids of higher viscosity but similar surface tension (n-heptadecane, C17:  $\rho=777 \text{ kg}\cdot\text{m}^{-3}$ ,  $\sigma=27.5 \text{ mN}\cdot\text{m}^{-1}$ , and  $\nu=4.8 \text{ cSt}$ ; Silicone Oil, S5:  $\rho=910 \text{ kg}\cdot\text{m}^{-3}$ ,  $\sigma=20 \text{ mN}\cdot\text{m}^{-1}$ , and  $\nu=5 \text{ cSt}$ ; and Silicone Oil, S100:  $\rho=960 \text{ kg}\cdot\text{m}^{-3}$ ,  $\sigma=20 \text{ mN}\cdot\text{m}^{-1}$ , and  $\nu=100 \text{ cSt}$ ). As mentioned earlier, the complex dynamics of the gas layer evolution reported here arise from the interplay of capillary waves on drop and liquid surfaces, which would be significantly damped for high viscosity liquids. Here, we compare the gas layer profiles for impact on the deep pool where the drop and film deformations are not restricted by the bottom substrate. We first note that the gas layer profiles in the approaching and rebounding stages are qualitatively similar between C14 (3.6 cSt) (Fig. 3e-f) and C17 (Fig. 5a-b). For significantly high viscosity S100 (Fig. 5c-d), however, the capillary waves on both drop and liquid surfaces decay quickly and as such the rich dynamics in the gas layer profile disappear. The profiles maintain the bell-shape with minimal changes in thickness throughout the approaching and rebounding stages.

To further delineate the effects of drop and liquid surfaces on the gas layer dynamics, we purposefully weaken the capillary waves either in the drop or in the liquid film by mismatching

their viscosities. For the first configuration of a low viscosity drop (S5) impacting on a high viscosity liquid pool (S100), no interference fringe was observed during the rebounding stage. This signifies rapid rebound of the drop from the liquid surface without further interaction. Since high viscosity dissipates the kinetic energy and weakens the capillary wave, the liquid surface recovers much slower than the drop, causing a large gap between them. It shows that in order for observable fringes to form during the rebounding stage, it is imperative that the drop and liquid surfaces recover at similar speeds. For the second configuration of high viscosity drop (S100) impacting on low viscosity pool (S5) (Fig. 5e-f), the capillary wave in the drop is significantly weaker. Consequently, in the rebounding stage we observe formation of the neck region in the rim propagating to the center, similar to the dynamics observed for C14 and C17. The similarity among features observed for C14, C17 and S100 (drop)/S5 (pool) and the minimized variation in the gas layer dynamics for S100 (drop)/S100 (pool) suggest that the capillarity or surface wave in the liquid film indeed plays a critical role in creating gas layer morphologies different from the traditional bell-shaped (dimple) profiles.

The important role of liquid surface capillarity on the gas layer dynamics is further highlighted by comparing the impact on solid surface (Fig. 11 (b1) (b2) from reference [11]) and thin film (Figs. 3a-b). While the gas layer thickness profiles are bell-shaped for both cases during the approaching stage, the profile becomes comparatively thinner and flatter for impact on the thin film due to the adaptive liquid surface that moderates pressure buildup. Furthermore, during the rebounding stage, the radial profile for the thin film develops a dimple at the rim, whose thickness can be larger than that at the center, which is absent for impact on the solid surface. The rim dynamics indicates the interaction between the drop and the deformed liquid surface.

In summary, we have investigated the evolution of the gas layer thickness profile when a drop bounces upon impacting liquid surfaces of various film thicknesses and Weber numbers, leading to the observation, quantification and explanation of several phenomenologically new and significant features. We have demonstrated that the deformable liquid surface absorbs the impact inertia and morphs itself to moderate the pressure gradient and generate surface waves. As a result, the bell-shaped profile, which is universal and omnipresent for impact on solid surfaces, is found to transform into new shapes such as the “annular dimple” at the rim and the “reversed bell-shape”, signifying interaction between the drop and the film surface.

## **References**

- [1] A. Yarin, *Annu. Rev. Fluid Mech.* **38**, 159 (2006).
- [2] C. Josserand and S. Thoroddsen, *Annu. Rev. Fluid Mech.* **48**, 365 (2016).
- [3] J. M. Kolinski, S. M. Rubinstein, S. Mandre, M. P. Brenner, D. A. Weitz, and L. Mahadevan, *Phys. Rev. Lett.* **108**, 074503 (2012).
- [4] J. de Ruiter, J. M. Oh, D. van den Ende, and F. Mugele, *Phys. Rev. Lett.* **108**, 074505 (2012).

- [5] M.-J. Thoraval, K. Takehara, T. G. Etoh, S. Popinet, P. Ray, C. Josserand, S. Zaleski, and S. T. Thoroddsen, *Phys. Rev. Lett.* **108**, 264506 (2012).
- [6] M. Pack, H. Hu, D. Kim, Z. Zheng, H. Stone, and Y. Sun, *Soft Matter* **13**, 2402 (2017).
- [7] D. Richard and D. Quéré, *Europhys. Lett.* **50**, 769 (2000).
- [8] J. C. Bird, R. Dhiman, H.-M. Kwon, and K. K. Varanasi, *Nature* **503**, 385 (2013).
- [9] J. Kolinski, L. Mahadevan, and S. Rubinstein, *Europhys. Lett.* **108**, 24001 (2014).
- [10] J. de Ruiter, R. Lagraauw, D. van den Ende, and F. Mugele, *Nat. Phys.* (2015).
- [11] J. de Ruiter, R. Lagraauw, F. Mugele, and D. van den Ende, *J. Fluid Mech.* **776**, 531 (2015).
- [12] R. C. van der Veen, T. Tran, D. Lohse, and C. Sun, *Phys. Rev. E* **85**, 026315 (2012).
- [13] R. C. van der Veen, M. H. Hendrix, T. Tran, C. Sun, P. A. Tsai, and D. Lohse, *Soft Matter* **10**, 3703 (2014).
- [14] M. M. Driscoll and S. R. Nagel, *Phys. Rev. Lett.* **107**, 154502 (2011).
- [15] Y. Liu, P. Tan, and L. Xu, *J. Fluid Mech.* **716**, R9 (2013).
- [16] E. Li and S. T. Thoroddsen, *J. Fluid Mech.* **780**, 636 (2015).
- [17] W. Bouwhuis, R. C. A. van der Veen, T. Tran, D. L. Keij, K. G. Winkels, I. R. Peters, D. van der Meer, C. Sun, J. H. Snoeijer, and D. Lohse, *Phys. Rev. Lett.* **109**, 264501 (2012).
- [18] S. Wildeman, C. W. Visser, C. Sun, and D. Lohse, *J. Fluid Mech.* **805**, 636 (2016).
- [19] Y. Couder, E. Fort, C.-H. Gautier, and A. Boudaoud, *Phys. Rev. Lett.* **94**, 177801 (2005).
- [20] S. Thoroddsen, M.-J. Thoraval, K. Takehara, and T. Etoh, *J. Fluid Mech.* **708**, 469 (2012).
- [21] T. Tran, H. de Maleprade, C. Sun, and D. Lohse, *J. Fluid Mech.* **726**, R3 (2013).
- [22] B. Ching, M. W. Golay, and T. J. Johnson, *Science* **226**, 535 (1984).
- [23] H. N. Oguz and A. Prosperetti, *J. Fluid Mech.* **219**, 143 (1990).
- [24] J. Zou, P. F. Wang, T. R. Zhang, X. Fu, and X. Ruan, *Phys. Fluids* **23**, 044101 (2011).
- [25] K.-L. Pan and C. K. Law, *J. Fluid Mech.* **587**, 1 (2007).
- [26] X. Tang, A. Saha, C. K. Law, and C. Sun, *Soft Matter* **12**, 4521 (2016).
- [27] P. D. Hicks and R. Purvis, *Phys. Fluids* **23**, 062104 (2011).

## **Publications**

- X. Tang, A. Saha, C.K. Law, Chao Sun, Bouncing Drop on Liquid Film: Dynamics of Interfacial Gas Layer (under review)
- X. Tang, A. Saha, C.K. Law, Chao Sun, Role of Viscosity in Bouncing vs Merging Transition for Drop impact on Liquid Film (in preparation)